ISSN 1392-1320 MATERIALS SCIENCE (MEDŽIAGOTYRA). Vol. XX, No. X. 2027

Freeze-thaw Performance and Microstructural Mechanisms of Hybrid OPC-Alkali Activation as a Route to Durable Red Mud-based Non-Fired Bricks

Abdul MAJID [1, 2], Lei WU [1, 2], Zhe SUN [1, 2], Yanan DAI [3], Tianjiao ZHANG [3], Yan CAO [1, 2, 3, 4, 5, 6 *]

[1] *College of Chemistry and Chemical Engineering, Anhui University, 230601, Hefei, China*
[2] *Guangzhou Institute of Energy Conversion, Chinese Academy of Sciences, 510640, Guangzhou, China*
[3] *Shandong Laboratory of Aluminum Advanced Manufacturing in Binzhou (SLAAMB), Binzhou Institute of Technology, Weiqiao-UCAS Science and Technology Park, Binzhou*
[4] *University of Science and Technology of China, 230026, Hefei, China*
[5] *CAS Key Laboratory of Renewable Energy, 510640, Guangzhou, China*
[6] *Guangdong Provincial Key Laboratory of New and Renewable Energy Research and Development, 510640, Guangzhou, China*

http://doi.org/10.5755/j02.ms.44232

Received 2 February 2026; accepted 19 March 2026

This paper discusses the increasing issues of urbanization and industrialization by creating compressed non-fired solid waste bricks (CNFSWB) under 10 MPa uniaxial pressure and without heat treatment with red mud (RM), fly ash (FA), and silica fume (SF) as the main materials with less ordinary Portland cement (OPC) and alkali (NaOH) activation, providing an alternative construction material which is sustainable. Effects of combinations of OPC-NaOH on early-age and 28-day compressive strength were also systematically examined, as well as their freeze-thaw resistance in order to determine durability behavior under cyclic environmental factors. Findings indicate that cement hydration and alkali activation have a synergistic effect on mechanical performance, leading to enhancement of the dissolution of aluminosilicate phases and consequent formation of C–S–H, C–A–S–H and N–A–S–H gels. The specimens with a moderate level of NaOH dosage (8.4 g) had the highest 28-day compressive strength (52.24 MPa) and better freeze-thaw resistance, which showed that there is an optimal level of OPC content and alkali activation ratio, which is important in densifying the microstructure, mechanical strength and long-term stability. These results indicate the possibilities of using strategic blending of industrial solid wastes with controlled chemical activation in the production of sustainable, high performance, and durable non-fired bricks to be used in construction.
Keywords: geopolymerization, alkali activation, industrial waste utilization, sustainable building materials, low-carbon binder.

1. INTRODUCTION

As the industrial activity of the world increases in pace, the pressure on the ecological environment is increasing. One of the greatest environmental management issues in contemporary times is industrial solid waste [1]. The amount of solid waste produced continues to increase as the industrial sectors expand and now, it acts as a source of significant land cover and poses a risk to the ecological and human security [2]. In the era of the natural resources and energy reserves depletion, the transformation of solid waste into a recoverable resource is not an option anymore, it is a necessity.

China is currently generating about 899 million tons of FA and 107 million tons of RM, as recent industry reports indicate [3]. In spite of this, RM and FA have not been born into building materials yet because of technical issues. High alkalinity and low reactivity of RM may lead to dimensional instability and undeveloped mechanical strength. Untreated RM-based materials have a compressive strength which is normally a third of that of OPC after 28 days of curing [4, 5]. Interestingly, RM holds Al_2O_3 and Fe_2O3 in abundance, whereas FA is rich in Al_2O_3 and SiO_2, meaning that there may be potential synergistic reaction pathways which form AFt-like mineral phases in theory [6, 7]. But simple RM-FA mixtures are usually compromised by low early-age strength and slow hydration kinetics, which produce low compressive strength. This is because of the low supply of reactive Al^{3+} in red mud and the comparatively low reactivity of FA at young ages to adsorb onto hydration products, and thus retards the hydration-inducing process further. As such, it is important to use effective activation schemes to improve the performance of these composite materials. The primary reason why SF, which is a by-product of the ferrosilicon alloy production have received a lot of attention with regard to its potential application in cementitious systems is its unique physicochemical characteristics. High specific surface area ($15-30$ m^2/g), particle size, and containing more than 90% amorphous SiO_2 [8] with an ultrafine particle size. Despite the generally recognized filler and pozzolanic effects of SF, its mechanism in activating the reactivity of low-activity industrial residues is not well studied. Recent studies put forward the idea that SF not only introduces reactive silica to enhance the kinetics of hydration but also modulates the Si/Ca ratio in the hydration matrix and thereby helps in

* Corresponding author: Y. Cao
E-mail: *caoyan@ms.giec.ac.cn*

refining the structure of hydration products formed [9]. SF reacts with surface hydroxyl groups and ions including Mg^{2+}, Ca^{2+}, and Al^{3+}, which stimulates the formation of other gel products and the dissolution of active components in the waste residue of industries [10 – 12].

Scientists have explored the possibility of brick replacement or modalities of using different waste materials in the manufacture of bricks. It has been established that geopolymer technology is an effective way of converting the aluminosilicate-based wastes into useful construction materials [13]. It has been found that FA [14], bottom ash [15], granulated blast furnace slag [16], rice husk ash [17], RM [18], and ceramic dust waste could all be used as raw materials in the manufacture of geopolymer bricks [19]. Inorganic materials that have the characteristics of ceramics are geopolymers, which are produced by the reaction of the aluminosilicate sources with the alkaline solutions at room temperature or controlled moderately higher temperatures. Some of the strategies to minimize these emissions are process optimization, carbon capture and storage and use of alternative cementitious materials [20 – 23].

High-pozzolanic industrial aluminosilicate solid wastes like RM, FA, and SF, which have comparable chemical properties to Portland cement stages, have been extensively studied as an alternative to cementitious material with low carbon levels construction [24, 25]. Hydration in blended binders occurs in two phases: primary cement hydration to form $Ca(OH)_2$, and secondary pozzolanic hydration of $Ca(OH)_2$ with the reactive waste products. The pH, chemical composition, and reactivity of industrial wastes produced in various processes, however, are highly variable and excess replacement levels tend to result in decreased early-age strength because of inadequate availability of $Ca(OH)_2$ [26, 27] and may cause toxicity among other things . In order to overcome such limitations, chemical activation has been suggested to be used to increase the reactivity of waste and to elevate the mechanical performance [28 – 30]. The usual activators are NaOH, Na_2SO_4, CaO, and $Ca(OH)_2$ each with different activation effects [31 – 33]. Alkali activators and in particular, NaOH have been found to increase the compressive strength of the high-volume waste system considerably by increasing the rate of aluminosilicate dissolution and the formation of gels [34 – 37]. Besides, the alkali-activated system allows the efficient use of industrial wastes and a decrease in the consumption levels of clinker and CO_2 emissions, which provides a sustainable alternative to the standard cement-based products [38 – 42].

The two most popular types of bricks are fired and unfired bricks used in construction globally, but most of the unfired bricks are made by stabilizing soil or sand using binders like cement or lime [43]. The fired clay bricks are mostly made of clay, sand, and water in certain ratios. Fired clay bricks production is a very energy-intensive process [44], and it is estimated that 24 million tons of coal are used each year. It is also a process that produces a lot of air pollution [45], and solid waste. Conversely, the production of the unfired bricks is a cleaner and more environmentally friendly process since they do not have to be fired at a high temperature. They are, however, commonly dependent on the Portland cement or lime to be used as stabilizing agents. The energy required to make these binders is energy consuming and contributes significantly to greenhouse gas emissions, such as CO_2 [45]. To overcome these drawbacks, extensive research over the past two decades has focused on identifying alternative, eco-friendly raw materials for construction. In a bid to beat these weaknesses, there have been two decades of research on finding alternative raw materials that are environmentally friendly to be used during construction. Actually, the most promising opportunities include industrial by-products and wastes, which can partially or entirely substitute the conventional materials, enhance some technical properties, satisfy the performance demands, and bring about sustainable development [46 – 49].

The use of industrial by-products in manufacturing of bricks not only improves the performance of the bricks mechanically, it also minimizes landfill wastes and the carbon footprint that is realized by the traditional fired bricks. The proportions of these wastes, as well as the controlled activation of OPC to NaOH, are important elements with regard to the realization of structural integrity and long-term durability. This paper examines how RM, FA, and SF work together to enhance the microstructure, compressive strength, and freeze-thaw resistance of compressed non-fired bricks, both in terms of sustainable waste management and resource-efficient construction. The results are informative in designing superior, long-lasting and low-carbon construction substances to promote more eco-friendly construction.

2. MATERIALS AND METHODS

2.1. Materials

The cementitious systems were developed using three representative industrial by-products as RM, FA, and SF that were used in this study. The OPC (P.O 42.5) to be used in mixtures was provided by Hefei Changfeng Conch Cement Co., Ltd., and FA, RM, and SF were acquired in domestic coal-fired power stations and alumina refineries of the aluminum enterprises, respectively. Fig. 1 indicated that the RM was fine with a characteristic brownish-red coloration, but silica fume was a fine cold-grey powder. The fly ash was made up of fine, spongy particles of light grey color with smooth surfaces, which pointed it to the fact that fly ash was largely vitreous. Fig. 1 illustrates the morphology of RM, FA, SF, and OPC.

Table 1 indicates the chemical makeup of the raw materials that were used in this study. FA is mainly made of Al_2O_3 and SiO_2, which constitute 83.50 % of its composition, with Fe_2O_3 coming in second at 2.92 %. On the other hand, Fe_2O_3 is the predominant mineral in RM constituting 57.23 % of the mineral and the combination of Al_2O_3 and SiO_2 forms 27.23 % of its composition. On the same note, SF mostly consists of SiO_2 that constitutes about 97.2 percent of its total composition. The rest of silica fume is composed as Al_2O_2, Fe_2O_3 and CaO that are approximately 1-2, 0.5-1 and 0.5-2. This composition is due to the peculiarities of each material, and silica fume is very active, thus, the mechanical strength and long-term effectiveness of cementitious composites are highly enhanced. The CaO content of OPC (43.78) is high, and the fractions of SiO_2 and Al_2O_3 are also significant in this case, as it is a calcium-rich hydraulic binder.

a b c d

Fig. 1. Morphology of : a – red mud; b – fly ash; c – silica fumes; d – ordinary Portland cement

Table 1. Main raw materials FA, RM, SF and OPC Chemical composition (wt.%)

Materials	Na_2O	MgO	Al_2O_3	SiO_2	K_2O	CaO	Fe_2O_3
FA	0.66	0.40	27.70	55.80	1.23	0.88	2.92
RM	5.00	0.26	21.85	5.38	0.41	3.19	57.23
SF	0.11	0.51	0.10	97.20	0.81	0.21	0.01
OPC	0.35	2.84	10.28	22.79	1.12	43.78	2.72

Preparation of the specimen was done with laboratory tap water that met the Chinese Standard GB 57492022. The alkaline activator used was NaOH of analytical grade, which was provided by Shanghai Macklin Biochemical Technology Co., Ltd.

The particle size distributions of all the raw materials were measured with a Microtrac S3500 laser diffraction analyzer and the results are provided in Table 2 and Fig. 2. Particle sizes used were 2.31 – 31.11 μm RM, 3.27 – 37.00 μm FA, 4.62 – 18.50 μm SF, and 5.50 – 52.32 μm OPC. Median size (d_{50}) (11.00 μm) of SF was a little less than in RM and FA (13.08 μm), whereas OPC had a much larger median size (22.00 μm). The fine fraction (d_{10}) of RM (2.31 μm) was lower than that of FA, SF, and OPC, which meant that it contained more ultrafine particles. Conversely, OPC (52.32 μm) had the highest value of the coarse fraction (d90), followed by FA (37.00 μm), RM (31.11 μm), and SF (18.50 μm). In general, SF had the smallest particle size distribution and fineness and can therefore be effectively used in the activation of non-fired brick systems as a calcium-based activator.

2.2. Preparation procedure of cementitious material

A set of preliminary experiments were carried out prior to finalizing the mix proportions that were to be used in Table 3 to methodically analyze the effect of important parameters at a constant uniaxial compaction pressure of 10 MPa. For instance, the NaOH content was focused on, and it is a critical parameter that affects the reaction environment and strength development and surface stability of CNFSWB. Various doses of NaOH were explored to produce a good balance between alkali activity and matrix stability and reduce the chances of efflorescence and surface corrosion. Though an increase in alkali contents facilitated early aluminosilicate phases dissolution, excessive use of NaOH led to surface crystallization and a microstructure unstable to the crystal. Furthermore, a small quantity of OPC was added to the hybrid formulations so as to strengthen early and to promote bonding of the microstructure without reducing the advantages of alkali activation.

Table 2. Particle size distribution of raw materials

Parameters	RM	FA	SF	OPC
Particle size range, μm	2.31 – 31.11	3.27 – 37.00	4.62 – 18.50	5.50 – 52.32
d_{10}, μm	2.31	3.27	4.62	5.50
d_{50}, μm	13.08	13.08	11.0	22.0
d_{90}, μm	31.11	37.00	18.50	52.32

Table 3. Experimental mix design

S. No	Pressure applied, MPa	RM, wt.%	FA, wt.%	SF, wt.%	OPC, wt.%	Water, g	10M NaOH, g
CNFSWB-0	10	30	50	20	–	21	–
AA-CNFSWB	10	30	50	20	–	11.2	9.8
OPC-CNFSWB	10	27	45	18	10	21	–
H1-CNFSWB	10	27	45	18	10	18.2	2.8
H2-CNFSWB	10	27	45	18	10	15.9	5.1
H3-CNFSWB	10	27	45	18	10	12.6	8.4
H4-CNFSWB	10	27	45	18	10	9.8	11.2

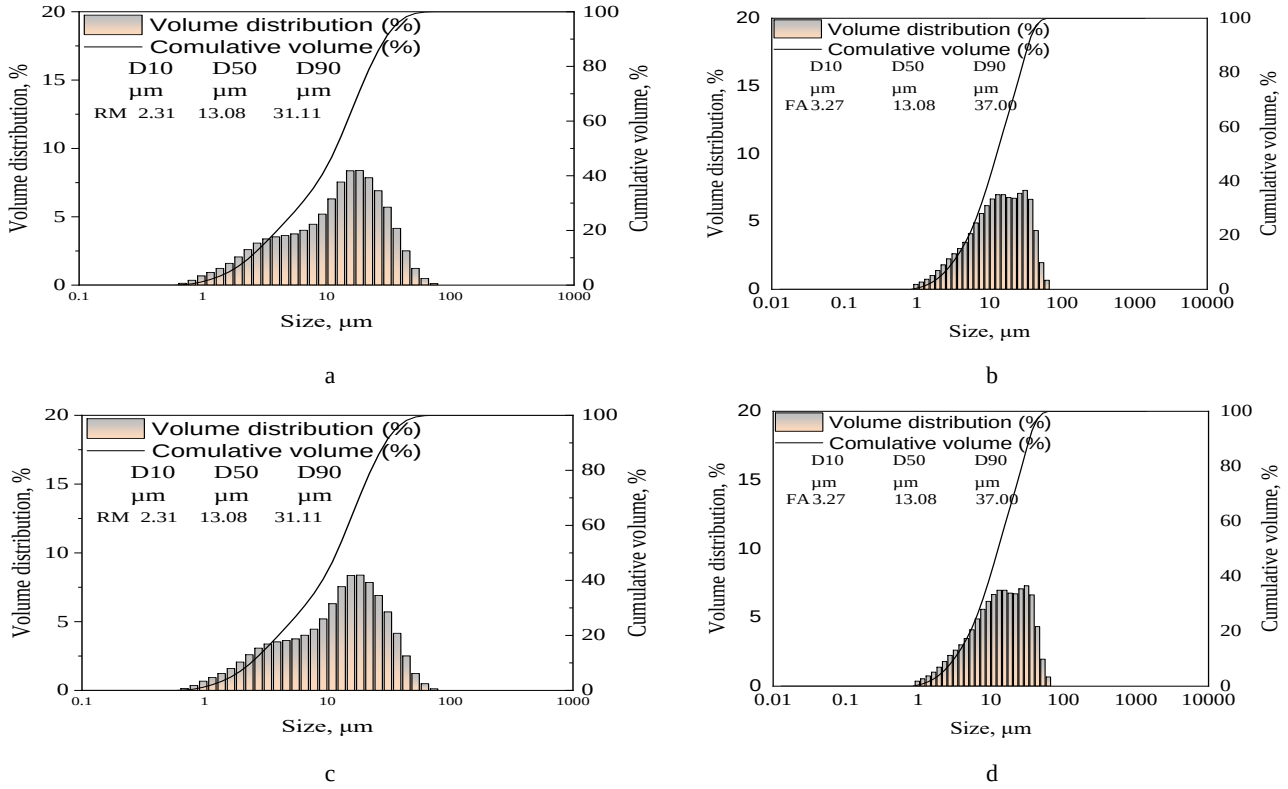

Fig. 2. Particle size distribution of : a – red mud; b – fly ash; c – silica fumes; d – ordinary Portland cement

A mixed evaluation of the mechanical performance, microstructural integrity, and surface condition allowed the selection of the 10 M NaOH concentration with the optimal dosage range and the minimum OPC content in AA-CNFSWB and hybrid formulations. This was because of the controlled alkali content and the restricted amount of OPC that allowed effective activation, structural integrity and reduced efflorescence. The gradual optimization effort allowed the stabilization of the reaction conditions in all mixes, and accurate comparison of mechanical performance and durability of non-activated, alkali-activated, OPC-activated, and hybrid CNFSWB systems.

RM, FA, and SF were dried at 105 ℃ over a period of 24 hours to obtain a constant mass and to remove all the remaining moisture. Each raw material was dried, and then weighed precisely with respect to the mix proportions of the various components as shown in Table 3.

The nomenclature of the samples was determined by the kind of binder system and the method of activation used by the composite bricks. CNFSWB refers to solid waste bricks that are compressed and non-fired and made using RM, FA, and SF. The suffix -0 indicates the control specimen that has neither a chemical activator nor cement. AA-CNFSWB is based on the alkali-activated specimens, where a 10 M NaOH solution has been employed as the activator in the absence of the OPC. OPC-CNFSWB implies specimens that are made with OPC as the only binder. H1-CNFSWB through H4-CNFSWB are hybrid binder systems where OPC is mixed with different contents of various proportions of alkali activator (10 M NaOH) and water content and the numerical index (H1-H4) indication of the system is lower water content and higher NaOH content.

The mixing was performed with the help of a laboratory-grade mechanical mixer, but some preliminary experiments were carried out to maximize the proportioning of the material and the order of mixing under a constant compaction pressure of 10 MPa since the pressed brick mixtures had little water requirement and tended to be dry-consistent. The amount of water was deliberately minimized to make the mixture semi-dry to press, instead of a flowing paste. The dry-mixed constituents in both formulations were initially mixed in low speed for 3 min to achieve homogeneity. Where necessary, water and NaOH solution were added slowly with the mixture stirring to ensure uniform wetting and also to discourage local agglomeration. The mixture was then mixed further, at a low power of about 30 s where it was given time to redistribute moisture and scrape the material stuck on the walls of the vessel to a uniform granulated consistency fit to be compacted.

The mixtures were finely compacted by an automatic hydrostatic press of bricks to a uniaxial constant pressure of 10 MPa. The load was then applied slowly at a steady rate of 0.5 kN/s to a peak force of 16 kN so that the densification was uniform and the internal defects were minimized. The compaction process resulted in compact and homogenous pressed blocks with stable geometry. Three cubic specimens of size 40 mm × 40 mm × 40 mm were made with each mix formulation to make the process reproducible and accurate in measuring the compressive strength. Moreover, there were also different groups of specimens with the same dimensions and proportions of mix to be used in freeze-thaw cycling experiments, so that the assessment of durability could be carried out without affecting the specimens to test the mechanical strength.

The specimens were demolded and then, they were cured under a controlled temperature of 20 ± 2 ℃ and in excess of 95 percent relative humidity to test the progress of mechanical strength and microstructural development over a duration of 3, 7 and 28 days. One of the sets of specimens was subjected to freeze-thaw cycling tests after 28 days of curing to determine the durability performance and the rest were subjected to mechanical and microstructural tests.

For microstructural and physicochemical analyses, hydration was terminated by immersing representative specimens in 95 % ethanol for 48 h to halt ongoing reactions. The samples were subsequently vacuum-dried at 60 °C for 24 h to remove residual moisture. Dried specimens were then sectioned as required for detailed microstructural, mineralogical, and spectroscopic characterization. Fig. 3 presents the schematic view of the proposed study.

2.3. Test methods

2.3.1. Compressive strength

The testing procedure prescribed for the determination of the compressive strength of the samples is in accordance with the Chinese standard GB/T 17671-2021 [50] on methods of testing cements. Determination of strength, commonly used in China for performing tests on compressive strength characteristics of cement-based materials. The constant-stress cement pressure testing machine DEY-300 is used for maintaining the same level of stress that makes the results accurate. It is possible to perform this type of test using prismatic specimens (40 mm × 40 mm × 40 mm) due to the stress balance of the prism-shaped body under compression. The curing periods of 3, 7 and 28 days encompass the usual phases of hydration in the cementitious materials.

Early age (3 days) testing provides information about the early setting and hardening properties of the material, while 7- and 28-days test results are used to determine the long-term characteristics of the material.

A standard of 3 replicates per group is chosen to verify statistical results. The average value shows the most likely average for all of the samples and can be considered as a central tendency data while standard deviation is considered as compatibility for each compressive strength between samples. This statistical technique gives independent results concerning the behavior of the material and their reproducibility. The mixture of various curing ages also led to a holistic approach to the strength development as a time-dependent factor that is needed to be potentially applied in the construction.

2.3.2. Fourier transform infrared spectroscopy

The samples used in the described process were first dried at 105 ℃ during 3 h prior to the collection of the spectrum so that moisture would not have a negative impact on spectral collection. This measure will help ensure that actual chemical composition of the sample, rather than water and other volatile substances, is in agreement with the FT-IR results. The product that was dried was subjected to additional treatment in the form of KBr preparation to analyze it. KBr, on the other hand, is an IR transparent and the beam of infrared passes through the sample. A fine suspension of KBr is added to the sample, and pressed as a pellet. The frequency of FT-IR spectra was measured using a Shimadzu FTIR-8400S. This spectrometer covers the infrared test range, which is $4000 - 400\ cm^{-1}$, which is widely used with identification of various functional groups of the sample. Its $1cm^{-1}$ resolution makes it able to identify the area fine and accurately the area with high absorption peaks which depicts vibrational frequencies of various bonds in the chemical structure of the sample.

2.3.3. X-ray diffraction analysis

The powdered sample in this process was first dried at a temperature of 105 ℃ in a period of 3 h to dry out all moisture that can affect the diffraction data. An X-ray diffractometer was used to measure XRD with a Rigaku SmartLab 9 kW. The device was set to operate at normal conditions of 40 kV and 40 mA current to give a high intensity X-ray needed in crystal structure study. The X-ray source of CuKalpha radiation (1.5418 ºA) which is universally used to interact with the crystal lattice of the sample was used. A 2theta range of 5 – 70 degrees was utilised, which encompasses a wide range of the possible diffraction peaks of various crystalline phases. A scan rate of 50º/min was used, which is a good tradeoff between analysis time and resolution.

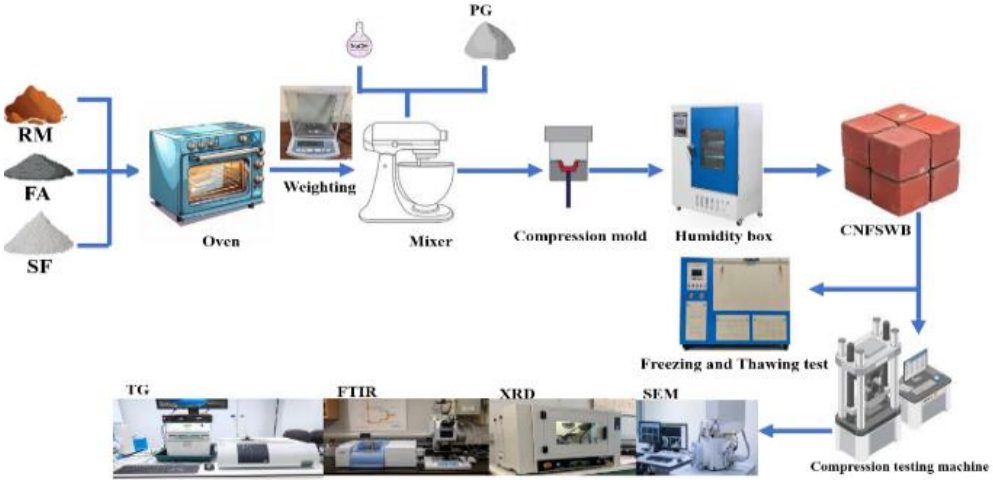

Fig. 3. Schematic illustration of the preparation process

The resulting diffraction pattern can be utilized in identifying mineral phases through a comparison with known reference patterns of characteristic reflection peaks. The comparison gives information on composition and crystallinity, etc.

2.3.4. Thermogravimetric analysis

Thermal profile and resultant mass loss of the hydration products in the samples were determined using thermogravimetric analysis (TGA) were performed TGA 5500 (TA Instrument, USA). Before the test, the samples were dried at 105 ℃ for 5 hours to eliminate moisture and sieved with 100 mesh sieve to obtain homogeneous particle size. The warm samples were analyzed by TGA heating them between 30 and 800 ℃ at a heating rate of 10 ℃/min. In these temperature regimes, one can uncover the various steps of mass loss connected to decay of the individual substances (water evaporation, carbonate disintegration and reconstitution or rupturing of hydration items such as calcium hydroxide or gypsum). Thermal curves would help identify the thermal stability and composition of the hydration products which provide information on chemical behavior of the material, and the structure development in the hydration state.

2.3.5. Scanning electron microscopy

Microstructures of the red mud-pulverized coal ash-silica ash ternary solid waste brick specimens were observed using a Hitachi S-4800 field emission scanning electron microscope. Before analysis, the seasoning samples were dried at 105 °C for 3 h to free the material of moisture deposits, purged with nitrogen gas to remove surface impurities, and gold-coated. The gold layer will not only expose the surface of the sample for direct SEM visualization but, it will also improve the conductivity of the sample to prevent any charging effects during imaging, events that are particularly important in HRSEM observations.

The SEM was operated at 20 kV, a value commensurable with both the obtaining of high-resolution images and the sufficient penetration depth of the electron beam into the sample surface. The microscope is equipped with the field emission, which offers a high resolution for observing the detailed microstructure including surface morphologies, particle distribution and interactions between particles.

2.3.6. Freeze-thaw cycle test

This test was conducted in accordance with the "Standard for Test Methods of Long-term Performance and Durability of Ordinary Concrete" (GBT 50082-2009) [51]. After curing the specimens for 28 days, they were immersed in water at (20 ± 2) °C for 4 days, with the water level 20 mm above the top surface of the specimens. After immersion, the specimens were removed, the surface water was wiped off, and the initial mass was recorded as M_0.

The specimens were then placed in a basket, and the basket was positioned at the center of the freeze-thaw chamber to start the freeze–thaw cycles. The freezing temperature was (−17 ± 2) °C. The specimens were frozen for 8 hours and then placed in water at (8 ± 2) °C to thaw for another 8 hours, completing one cycle. A total of 50 cycles were carried out. During the test, the specimen condition was observed and photographed.

The freeze-thaw resistance of the specimens was evaluated based on mass loss rate ($\Delta\omega_n$) and strength loss rate (Δf_c). The smaller the $\Delta\omega_n$ and Δf_c values, the better the freeze–thaw resistance of the specimens.

The strength loss rate after freeze–thaw cycles was calculated using Eq. 1:

$$\Delta f_c = \frac{(fc_0 - fc_n)}{fc_0} \times 100, \quad (1)$$

where Δf_c is the average freeze-thaw strength loss rate of the specimens after 50 cycles, %; fc_n is the average compressive strength after 50 freeze-thaw cycles, MPa; fc_0 is the average compressive strength of the reference specimens, MPa.

The mass loss rate after freeze-thaw cycles were calculated using Eq. 2:

$$\Delta\omega n = \frac{(G_0 - G_n)}{G_0} \times 100, \quad (2)$$

where Δωn is the average freeze-thaw mass loss rate of the specimens after 50 cycles, %; G_0 is the average mass of the specimens before the 50 freeze-thaw cycles, g; G_n is the average mass of the reference specimens after 50 freeze-thaw cycles, g.

3. RESULTS AND DISCUSSION

3.1. Compressive strength

The development of compressive strength of CNFSWB specimens prepared at a constant compaction pressure of 10MPa with various proportions of RM, FA and SF and varying activation routes is shown in Fig. 4 and Table 4. The findings indicate the existence of different strength development behaviors of non-activated, AA, OPC-activated, and hybrid activated systems. Section 2.3.1 provides details of the test procedure.

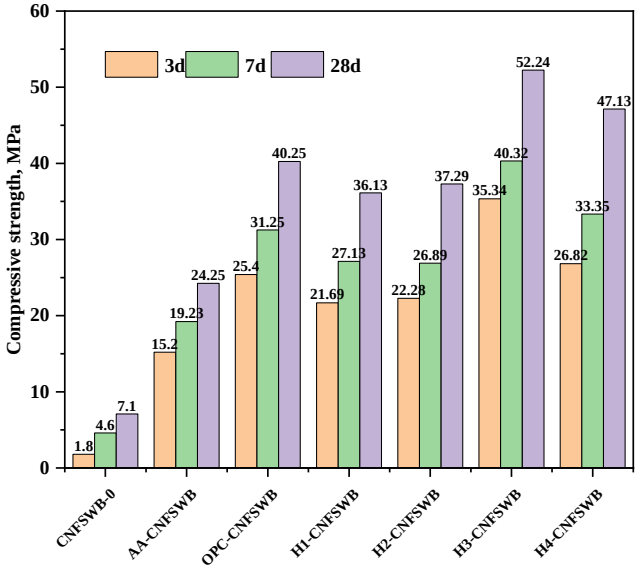

Fig. 4. Compressive strength of cementitious materials at 3,7, and 28 days

Table 4. Compressive strength of cementitious materials at 3,7, and 28 days

S. No	Compressive strength, MPa (3d)	Compressive strength, MPa (7d)	Compressive strength, MPa (28d)
CNFSWB-0	1.8 ± 0.09	4.6 ± 0.18	7.1 ± 0.25
AA-CNFSWB	15.2 ± 0.42	19.23 ± 0.55	24.5 ± 0.73
OPC-CNFSWB	25.4 ± 0.76	31.25 ± 0.94	40.25 ± 1.21
H1-CNFSWB	21.69 ± 0.61	27.13 ± 0.82	36.13 ± 1.05
H2-CNFSWB	22.28 ± 0.64	26.89 ± 0.79	37.29 ± 1.09
H3-CNFSWB	35.34 ± 1.12	40.32 ± 1.35	52.24 ± 1.67
H4-CNFSWB	26.82 ± 0.78	33.35 ± 1.02	47.13 ± 1.48

The compressive strength of the non-activated CNFSW sample was very low and it reached only 7.1 MPa at 28 days which supports that RM, FA, and SF alone have low self-cementing capacity when subjected to compaction but not with chemicals.

In the case of the AA-CNFSW, in which 10 M NaOH was the only activator and OPC was not included in the system, a significant strength gain could be detected in comparison to the non-activated sample. The compressive strengths obtained by the AA-CNFSW specimen were 11.2 MPa, 19.23 MPa and 24.25 MPa at 3, 7 and 28 days respectively. This strength increment is explained by the fact that the aluminosilicate phases of FA and SF dissolve under very alkaline environment, and after it, the gels of N -A-S-H type of geopolymers are formed. The lack of calcium however greatly inhibited the cross linking and densification of the gels hence relatively weak when compared to the systems made of OPC.

OPC-CNFSWB showed stable strength formation, with compressive strengths of 25.40 MPa, 31.25 MPa and 40.25 MPa of compressive strengths at 3, 7, and 28 days, respectively. This action is indicative of the heightened dominance of cement hydration reaction along with secondary pozzolanic reaction with RM, FA, and SF.

The compressive strength in hybrid activated systems was greatly dependent on the dosage of the NaOH. The strengths of the 28 days 36.13 MPa and 37.29 MPa of the NaOH contents of 2.8 g (H1-CNFSWB) and 5.1 g (H2-CNFSWB), respectively, were a bit lower than those of the OPC-only system. This implies that the alkalinity was low, which in part disrupted cement hydration without completely activating the aluminosilicate phases.

Strong increase in compressive strength was observed at a medium dosage of NaOH of 8.4 g (H3-CNFSWB) that produced the maximum 28-day strength of 52.24 MPa, and the speed of early age strength development. This higher performance is explained by the synergistic co-existence of C–S–H/C–A–S–H gels by cement hydration and N–A–S–H gels by alkali activation, forming a denser and more homogeneous matrix. In this system, early Ca^{2+} release from cement hydration enhances the dissolution of aluminosilicate phases under alkaline conditions, promoting the co-precipitation and intergrowth of C–S–H, C–A–S–H, and N–A–S–H gels. The interaction of this hydration and geopolymeric products results in the formation of a denser and more cross-linked gel network, which significantly improves the mechanical performance and structural integrity of the matrix. The addition of more NaOH to bring the level to 11.2 g (H4-CNFSWB) led to the loss of compressive strength in 28 days by 28.13 MPa. High alkalinity probably led to partial gel polymerization or to greater interconnection between the pores, or to microcracking of the gel due to the alkali, and the hardened matrix was weakened. In general, the findings indicate that NaOH-only is able to trigger geopolymerization, yet high strength in CNFSW systems is not obtained because of the limited calcium availability. Conversely, hybrid activation offers an ideal combination of hydration and geopolymerization processes resulting in high compressive strength in an event of the use of the correct amount of NaOH.

3.2. Structural and chemical characteristics in CNFSWB

Fourier transform infrared (FTIR) spectroscopy was used to examine the structural changes and chemical properties of the reaction products, which were generated in CNFSWB systems. After 28 days of curing the representative specimens, such as CNFSWB-0, AA-CNFSWB, OPC-CNFSWB, as well as the most advantageous hybrid mixture, H3-CNFSWB, were analyzed and the results are shown in Fig. 5. The comparative analysis will clarify the action of alkali activation, cement hydration, and the interaction between them on the bond evolution, gel formation and densification of the matrix. Section 2.3.2 gives the detailed procedure of the experiment.

The O-H stretch and H-O-H bending vibration of physically adsorbed and chemically bound water, respectively, are observed in a broad absorption band at the range 3426 – 3446 cm^{-1} and a weak band at the range 1587 – 1598 cm^{-1}, respectively [52, 53]. Such bands indicate products of hydration and geopolymerization, which consists of the presence of interlayer water in the amorphous gel networks of C–A–S–H and N–A–S–H. The fact that they persisted in all samples means that hydrated binding phases occurred during the curing in a wet environment.

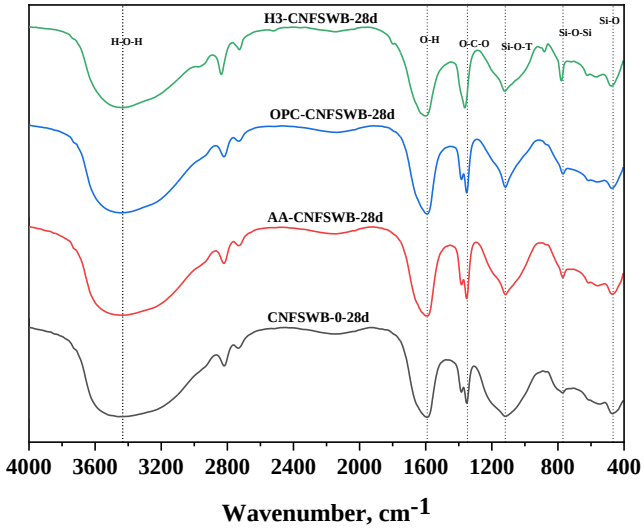

Fig. 5. FTIR spectra of ternary solid waste brick at 28d

Weak bands at 2817 to 2832 cm^{-1} are attributed to C-H stretching vibrations of the aliphatic CH_2/CH_3 groups, which are typically attributed to trace organic or carbonaceous impurities of red mud and fly ash. These

bands are not directly involved in the inorganic polymerization reactions and thus they vary insignificantly across the various activation systems. The asymmetric stretching vibration of carbonate (CO_3^{-2}) groups is the absorption band in the range of 1351 – 1357 cm^{-1}. This is mostly related to modicum normalization of calcium bearing hydration products through the curing and sample preparation process, at least in cement containing and hybrid systems, but a slight contribution by the remaining carbon in fly ash cannot be ruled out. The outstanding and the most structured part is the wide band between about 1116 and 1122 cm^{-1}, which is assigned to the asymmetric stretching vibrations of Si-O-T bonds (T = Si or Al) in aluminosilicate structures. This band is the fingerprint of the reaction between geopolymerization and hydration reaction and it signifies the formation of amorphous C-A-S-H and N-A-S-H gel networks [54]. This wide character is indicative of the structural disorder exhibited by the alkali-activated and hybrid cementitious materials, in both cases, concomitant incorporation of Ca^{2+} and Al^{3+} ions results in a mixed gel chemistry. This band is similar to all samples; it indicates that the general level of polymerization and the structure of the gel are similar.

There is a unique band at approximately 763 – 782 cm^{-1} that is ascribed to the symmetric stretching vibrations of SiO_2-Si and SiO_2-Al bonds that can occur either due to partially reacted silicate phases or unreacted crystalline minerals like the quartz sandwiched in fly ash and silica fume. This persistence of this band suggests that all silicate phases are not completely dissolved during activation, as is common in low temperature alkali-activated systems. The band at low wavenumbers at approximately 455 – 478 cm^{-1} is attributed to SiO bending vibrations in the tetrahedral silicate units [55 – 57].Overall, the FT-IR results demonstrate that alkali, cement, and hybrid activation routes all promote the formation of similar hydration and geopolymerization products in RM–FA–SF bricks. The dominance of Si–O–T vibrations, together with hydroxyl- and water-related bands, confirms that the mechanical performance of the bricks is governed by the development of amorphous aluminosilicate and calcium-aluminosilicate gels rather than by distinct crystalline reaction products. This conclusion is consistent with XRD and TG-DTG observations, which collectively indicate comparable gel-dominated binding mechanisms across all activation systems.

3.3. Transformation of hydrated products

The analysis using X-ray diffraction (XRD) was used to explain the evolution of the phases and crystalline attributes of the CNFSWB systems based on RM and FA and SF. Representative specimens were CNFSWB-0, AA-CNFSWB, OPC-CNFSWB, and H3-CNFSWB, which were also analyzed after 28 days of drying and the obtained diffraction patterns of these are shown in Fig. 6. The description of the experimental procedure is presented in Section 2.3.3. All the XRD patterns of the specimen show a complex of crystal reflections overlaying a wide diffuse halo which shows that the crystalline phases coexist with the dominance of an amorphous or poorly crystalline reaction matrix.

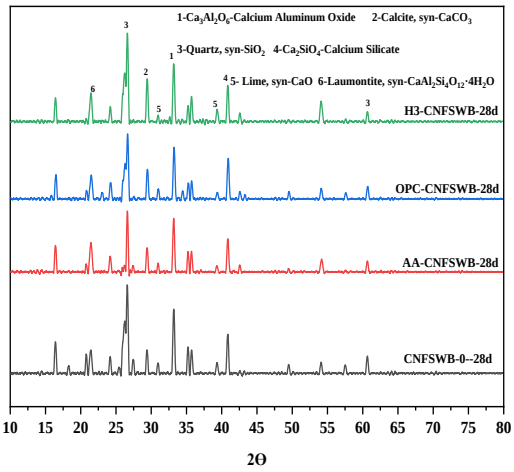

Fig. 6. XRD pattern of CNFSWB at 28 day

This hydrated background is typical of the hydration and geopolymerization derived gel phases which are incapable of being completely resolved by XRD and are however important in binding and strength building.

The phase identification confirms the existence of calcium aluminum oxide ($Ca_3Al_2O_6$), tricalcium aluminate ($Ca_3Al_{12}O_6$), quadrz (SiO_2), lime (syn-CaO), calcium silicate (Ca_2SiO_4), laumontite ($CaAl_2Si_4O_{12}\cdot 12H_2O$), calcite ($CaCO_3$), and gismondine ($CaAl_3Si_2O_8\cdot 4H_2O$). The low concentration of red mud could be the reason that some of the small crystalline phases are not mentioned in the RM-rich systems. The absence of RM can explain the fact that minor mineral phases were not detected [58].

The quartz reflections still exist at both curing ages in all the samples, which shows that there are still some crystalline silica impurities of fly ash and silica fume. Under the curing conditions used, largely this substance is not reactive, thus owing to its high thermodynamic stability which FTIR bands of unreacted silicate structures also affirm. The phases are calcium aluminum oxide and tricalcium aluminate formed as the result of the reaction between alumina-based components of red mud and fly ash. It has been found that these aluminate phases play a role in early-age kinetics of reactions and densification of matrices, especially in alkali-activated and hybrid systems.

The existence of silicate precursors in hydration reactions is indicated by the observed presence of Ca_2SiO_4. Though C–A–S–H and N–A–S–H gels are mostly amorphous, the presence of Ca_2SiO_4 indicates the continued polymerization of silicate and this is in line with the evidence of FTIR showing the formation of the SIO_{23} and SiO_{24} networks. This has been recognized as calcite, which is a result of partial carbonation of calcium bearing hydration products when preparing the samples and during the curing of the samples. It is usually found in cementitious and alkali-activated binders, and does not affect the integrity of the matrices. It is worth noting that, the existence of the zeolitic phases like laumontite shows that there is some crystallization of the aluminosilicate gels. These stages indicate that amorphous geopolymeric networks reorganize structurally under alkaline environments, which confirms reaction pathways of geopolymer-like in the CNFSWB systems.

3.3.1. Thermogravimetric analysis of hydration in CNFSWB

Thermal behavior and phase development of CNFSWB samples were analyzed with the help of thermogravimetric (TG) and derivative thermogravimetric (DTG) analyses. The representative samples, such as CNFSWB-0, AA-CNFSWB, OPC-CNFSWB and H3-CNFSWB were tested after 28 days of curing as shown in Fig. 7. Multi-stage mass-loss patterns are similar in the TG-DTG curves, which suggests comparable reaction products in all the activation systems whereas the differences in the intensity of mass-loss and the positions of the peaks indicate variation in gel composition and reaction.

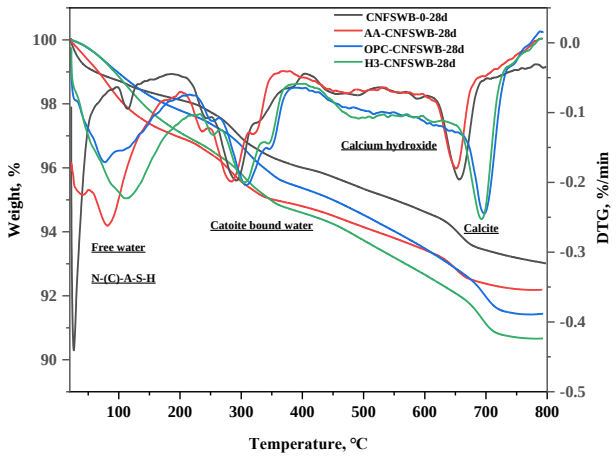

Fig. 7. TG-DTG curves of CNFSWB at 28 day

A second stage of mass-loss that follows between 220 and 350 °C is linked with the loss of chemically bound water associated with the reaction products, mainly C-A-S-H, N-A-S-H and N(C)-A-S-H gels [59, 61]. The peaks of the DTG in this region get wider and move to higher temperatures in the activated systems, particularly at 28 days, indicating gel polymerization and thermal stability following progressive incorporation of Ca_2+ and Al_3+ into the gel structure. The presence of a small DTG peak around 270 °C can be explained by the breakdown of katoite-type phases, which are created during initial reactions in hydration [62, 63].

At elevated temperatures, there is clear mass loss during 400 – 500 °C of OPC-CNFSWB and H3-CNFSWB, which is associated with the dissolution of calcium hydroxide ($Ca(OH)_2$) produced during cement hydration. This fact is demonstrated by the lower strength of this peak in the hybrid system than in OPC-CNFSWB, which shows that some of the $Ca(OH)_2$ was used up in secondary reactions with reactive aluminosilicate species, resulting in the occurrence of further C–A–S–H-type gels [64].

The last stage of mass-loss, which takes place in 550 – 750 °C, is explained by the breakdown of carbonate phases (primarily calcite) that were produced during the partial carbonation process of the curing and handling of samples [65]. The reduced carbonation observed in AA-CNFSWB and H3-CNFSWB compared to CNFSWB and OPC-CNFSWB due to denser gel matrices, and the higher usage of calcium-bearing phases during activation, which was confirmed by the XRD and FT-IR data. In general, the TG–DTG analysis proves that alkali, cement and hybrid activation play a significant role in dehydration behavior and thermal stability of CNFSWB systems. The gradual changes of the dehydration peaks to high temperatures and lowering of the $Ca(OH)_2$ and carbonate decomposition peaks in the later ages of curing show the formation of stable, gel-dominated binding phases. These results are in line with those of the FT-IR and the XRD analysis and the reason behind the enhanced mechanical performance and the durability of the activated CNFSWB specimens.

3.4. Microstructural morphology and distribution of hydration products

Fig. 8 shows the microscopic surface morphology of four typical CNFSWB samples, i.e., compaction-only sample (CNFSWB-0), alkali-activated sample (CNFSWB-ALK), cement-activated sample (CNFSWB-OPC), and the best hybrid sample H3-CNFSWB Fig. 8. These micrographs demonstrate that unique microstructural characteristics and binding mechanisms of various activation pathways appear. In Section 2.3.5, the detailed procedure used in testing is outlined. CNFSWB-0 sample Fig. 8 a shows a very tight structure, which mainly consists of mechanical bonds, and chemical bonds are not very evident. High uniaxial pressure is efficient in removing macro-voids resulting in a solid particle packing. Angular red-mud and spherical fly-ash grains, or cenospheric fly-ash grains, are trapped inside a fine particulate base, silica fume at the same time seems to be found in the form of dense agglomerations. Isolated block-like inclusions that are probably agglomerated ultrafine particles or broken cenospheres are encircled by thin interfacial cracks or crevices. Particle contacts are primarily point-to-point with little neck formation that forms weak interfaces that serve as stress concentrators. This microstructure reveals how the compressive strength of the compaction-only specimen and its durability did not prove to be very high.

The alkali-activated CNFSWB (CNFSWB-ALK) Fig. 8 b displays a distinct chemical binding mechanism dominated by alkali activation. Glassy fly-ash particles commonly exhibit thin reaction rims, and gel bridges are formed between adjacent grains. Silica-fume agglomerates are partially dissolved and overgrown by an amorphous N-A-S-H–type gel, with calcium supplied by red mud participating in the reaction. The gel appears as thin films coating particle surfaces and partially filling micro-voids.

However, a considerable fraction of particles remains unreacted or only partially reacted, and localized shrinkage, and microcracks are occasionally visible. Angular crystalline precipitates, likely sodium carbonates formed by carbonation of pore alkalinity, are also observed. Although alkali activation enhances chemical bonding relative to the compaction-only sample, the gel network is thinner and less continuous than in cement-activated systems, explaining its inferior mechanical performance and freeze–thaw durability. The cement-activated CNFSWB (CNFSWB-OPC) Fig. 8 c shows a markedly improved bonding environment. Hydration and pozzolanic reactions lead to the formation of foil-like and fibrillar C–(A)–S–H gel, which partially bridges adjacent particles and fills micro-voids. Interfacial gaps around inclusions are significantly reduced, and many particle contacts exhibit meniscus-shaped necks or gel collars.

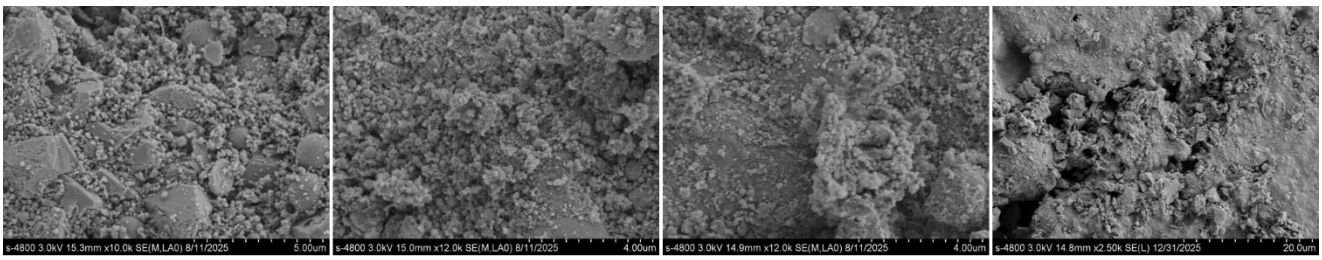

a b c d

Fig. 8. SEM micrographs of 28d samples of : a – CNFSWB-0; b – AA-CNFSWB; c – OPC-CNFSWB; d – H3-CNFSWB

Needle-like AFt hydrates are occasionally observed in residual pores, while some anhydrate cement grains persist as angular cores surrounded by porous hydration rims. Overall, the matrix transitions from purely mechanical interlocking to a combined mechanical-chemical bonding system, accounting for the enhanced strength and improved freeze–thaw resistance observed for CNFSWB-OPC. The optimal hybrid specimen H3-CNFSWB Fig. 9 d exhibits the most compact and homogeneous microstructure among all samples. A dense, continuous binding matrix is formed through the synergistic interaction of cement hydration products and alkali-activated gels. C–(A)–S–H and alkali-activated aluminosilicate gels intergrow and uniformly coat particle surfaces, effectively eliminating interfacial gaps and significantly reducing pore connectivity. Most fly-ash and silica-fume particles are well integrated into the matrix, with extensive neck formation and gel bridging between grains. Microcracks are rare, and residual pores are small and discontinuous. This highly densified microstructure strongly restricts water ingress and frost-induced damage, providing a clear microstructural explanation for the excellent mechanical performance and outstanding freeze-thaw resistance of H3-CNFSWB after 50 cycles.

3.5. Freeze-thaw cycle performance

The freeze-thaw cycle test was conducted to evaluate the durability of CNFSWB under simulated seasonal temperature fluctuations. After 28 days of standard curing, all specimens were subjected to a total of 50 freeze-thaw cycles, during which mass variation, compressive strength retention, and surface integrity were monitored. Mass loss and visible deterioration, including cracking, peeling, and spalling, were used as the primary indicators of freeze–thawresistance. The detailed experimental procedure is described in Section 2.3.6.

The OPC-CNFSWB was found to have the desirable freeze/thaw damage resistance and structural integrity without any apparent surface damage, despite the existence of up to 30 freeze-thaw cycles. Gradual degradation of the surface and mass loss were seen through further cycling after this point. Conversely, the AA-CNFSWB was only able to perform 20 cycles before cracking and peeling of surfaces started intensely, with a poor freeze thaw performance. In the case of the hybrid activated systems, a different behavior in terms of durability was noted.

Specimens H1-CNFSWB and H2-CNFSWB were stable structurally to 20 freeze-thaw cycles and then surface microcracks and localized spalling ensued. It is worth noting that the hybrid specimens with 8.4 g alkali (H3-CNFSWB) and 11.2 g alkali (H4-CNFSWB) showed a superior freeze thaw property whereby they remained intact, on all the 50 cycles without cracks formed and peeling surface with negligible loss of mass. This shows that a good cement-alkali synergy is useful in increasing densification of the matrix and durability in the long run during repeated freeze-thaw cycles.

Table 4 summarizes the degradation in compressive strength of CNFSWB due to freeze-thaw cycling. The compressive strength of AA-CNFSWB was significantly lowered after 20 freeze-thaw cycles, which implies low resistance to cyclic freezing. Beyond 20 cycles, the deterioration was severe and the specimen could not allow the structural integrity to be sustained in the presence of prolonged freeze-thawed conditions. Conversely, OPC-CNFSWB had superior durability, as it was observed that the mechanical performance of the material remained steady at 30 cycles, but thereafter, strength began to degrade steadily as the material was subjected to more cycling. Due to extensive cracking and fragmentation, no intact specimens remained for subsequent compressive strength testing; therefore, complete strength loss data could not be obtained for these mixes.

The compressive strength degradation of CNFSWB after freeze-thaw cycling is summarized in Table 5. In the hybrid cement alkali activated systems, it is worth mentioning that the hybrid specimens of the 8.4 g alkali (H3-CNFSWB) and 11.2 g alkali (H4-CNFSWB) had excellent freeze-thaw stability as they were structurally stable at all 50 cycles as shown in Fig 9. H3-CNFSWB had compressive strength of 48.16 MPa after 50 cycles with 7.81 strength loss and H4-CNFSWB had 42.50 MPa with strength loss of 9.82 indicating great resistance against mechanical degradation caused by freeze-thaw environment.

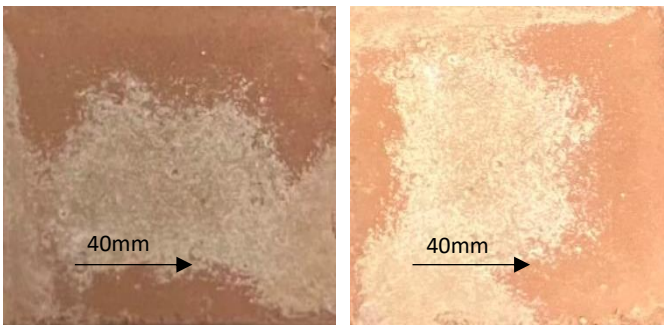

a b

Fig. 9. Morphology after 50 freeze-thaw cycle: a – H3-CNFSWB; b – H4-CNFSWB

Table 4. Influence of freeze-thaw cycle on compacted solidified soil

Specimen Number	Freeze-thaw-cycles	Specimen appearance state	Mass loss, %
CNFSWB-0	1	Breakage was observed	All
AA-CNFSWB	≤ 20	Breakage was observed	All
OPC-CNFSWB	≤ 30	Breakage was observed	All
H1-CNFSWB	≤ 20	Breakage was observed	All
H2-CNFSWB	≤ 20	Breakage was observed	All
H3-CNFSWB	≤ 50	only negligible mass loss	≤ 0.12
H4-CNFSWB	≤ 50	only negligible mass loss	≤ 0.53

Table 5. Data table of freeze-thaw cycle test results

No.	fc_0, MPa	Fc50, MPa	$\Delta\omega_n$, %	Δfc, %
CNFSWB-0	7.1	–	ALL	–
AA-CNFSWB	24.25	–	ALL	–
OPC-CNFSWB	40.25	–	ALL	–
H1-CNFSWB	36.13	–	ALL	–
H2-CNFSWB	37.29	–	ALL	–
H3-CNFSWB	52.24	48.16	0.38	7.81
H-4CNFSWB	47.13	42.50	>0.5	9.82

The deterioration behavior observed could be explained by the fact that CNFSWB structures are responding internally to repeated freezing and thawing. Squeezing increases the initial particle spacing between particles and increases interparticle contact leading to hydration and densification of the matrix, though it also causes residual internal stresses. In freeze-thaw cycling, water enters the pore net and loosely attached fine soil particles become softened when wet and break the adhesion between them.

Freezing of the pore water afterwards causes volumetric expansion that causes frost-related tensile and wedging stresses, which increase with each cycle, causing crack propagation on the surface, peeling of the surface, and loss of strength.

This is more pronounced in AA-CNFSWB in which slower reaction kinetics and less compact pore structure make things more prone to freeze-thaw damage.

Conversely, addition of cement with the correct amount of alkali facilitates development of a more compact and uniform microstructure which greatly minimizes infiltration of water and frost related damages. The high results of both H3-CNFSWB and H4-CNFSWB prove that the balanced cement-alkali synergy is effective to promote the freeze-thaw stability, but when cementation is insufficient, or pore connection is high, the cement eventually deteriorated under the cyclic freezing environment. The stability of hybrid hydration–geopolymeric gels under cyclic freezing and thawing, highlighting how a well-balanced C–S–H/C–A–S–H/N–A–S–H gel network improves structural resilience. In addition, the role of the interfacial transition zone (ITZ) has been incorporated, emphasizing its contribution to crack initiation and propagation under cyclic thermal stress. The effect of excessive alkali dosage has also been clarified, particularly regarding its potential to increase pore connectivity, reduce gel stability, and promote alkali-induced microcrack propagation, which collectively accelerate freeze–thaw deterioration. These additions provide a more systematic explanation of the durability differences observed among the tested specimens.

3.6. Hydration mechanism

The reaction mechanisms of (a) non-activated CNFSWB, (b) AA-CNFSWB, (c) OPC-CNFSWB, and (d) hybrid OPC–alkali CNFSWB reveal a progressive transition from physical bonding to hydration-dominated binding and finally to a highly efficient hybrid geopolymer–hydration system.

The CNFSWB system without chemical activators, RM, FA, and SF exhibits limited intrinsic reactivity. Upon water addition, slight dissolution of amorphous SiO_2 and Al_2O_3 from FA and SF occurs; however, the pore solution lacks sufficient alkalinity and calcium to sustain continuous geopolymerization or hydration reactions. Consequently, no stable cementitious gel network is formed. The hardened structure is mainly composed of mechanically compacted particles, where interparticle bonding is weak and discontinuous. This explains the very low compressive strength and slow strength development observed in non-activated CNFSWB.

The highly alkaline environment rapidly breaks Si–O–Si and Si–O–Al bonds in the amorphous phases of FA, SF, and partially RM, releasing silicate and aluminate species into the pore solution. These dissolved species react to polycondensation to produce sodium aluminosilicate hydrate (N–A–S–H) gel that serves as the major binding phase.

Considering that RM only adds small amounts of calcium, the total amount of Ca^{2+} is not enough to alter the geopolymer gel by a significant amount. Consequently, the N-A-S-H network is rather sodium rich, cross-linking has not occurred completely, and there has been minimal refinement of the pores. The gel applications are used to coat particle surfaces and partially seal voids to achieve moderate strength enhancement than inactivated system, and limit long-term densification and mechanical performance due to the absence of calcium.

$$SiO_2 + OH^- + H_2O \rightarrow [H_3SiO_4]^-; \quad (3)$$

$$Al_2O_3 + OH^- + H_2O \rightarrow [Al(OH)_4]^-; \quad (4)$$

$[H_3SiO_4]^- + [Al(OH)_4]^- + Na^+ \rightarrow N - A - S - H$ gel. (5)

The OPC-activated CNFSWB system is such that OPC triggers the hydration reactions when in touch with water. The disintegration and hydration of C_3S, C_2S, and C_3A phases produce calcium silicate hydrate (C–S–H), calcium aluminate hydrate (C–A–H), and calcium hydroxide. Constant calcium hydroxide development increases the pore solution pH parameter to about 1213, a factor that increases the rate of further cement hydration and dissolution of reactive silica and alumina present in RM, FA, and SF. The emitted Si^{4+} and Al^{3+} ions engage in secondary reactions of pozzolana with Ca^{2+} to produce more C–S–H and C–A–S–H gels. These hydration products slowly populate capillary pores, enhance interparticle contacts and enhance matrix continuity. Nevertheless, the total rate and connectivity of gels are still low in comparison with alkali-activated systems, so moderate strength develops.

$$SiO_5 + 7H_2O \rightarrow 3C - S - H + 3Ca(OH)_2; \quad (6)$$

$$SiO_2 + Ca(OH)_2 + H_2O \rightarrow 3C - S - H; \quad (7)$$

$$Al_2O_3 + Ca(OH)_2 + H_2O \rightarrow C - A - H. \quad (8)$$

NaOH is used rapidly in this system to enhance the rate of alkalinity, and dissolve amorphous aluminosilicate phases in FA, SF, and RM, at the same time providing calcium to the system through hydration of OPC. The dissolved silicate and aluminate species are polycondensed to make N–A–S–H gel, Ca^{2+} ions are involved in the making of calcium-modified gels like C–(A)–S–H. The partial intergrowth and coexistence of N–A–S–H and C–(A)–S–H gels makes one hybrid N–A–S–H–C–(A)–S -H binding network with high structural connectivity and chemical stability. These gels coat the particles uniformly, connect interfaces, and fill in micro-voids, which form a thick and crammed microstructure. The ultrafine particle size and high re-activity of SF further speed up the formation of gels by acting as nucleation sites and consuming CH rapidly therefore further refining microstructures. When alkali is properly balanced between sodium-based geopolymerization and calcium-based hydration, the early-age level of strength and high-quality long-term mechanical performance are reached. The over-alkalinity, on the contrary, alters the solidification of the gel as well as causes microstructural flaws, which underlie the necessity to optimize the dose of alkali. This hierarchical process proves that alkali activation is sufficient to trigger geopolymerization, but not high-strength because of the low amount of calcium and OPC hydration is moderately performes. The hybrid OPC-alkali activation process enhances the maximum gel formation and densification of the microstructure, and that is why the optimized CNFSWB bricks have high strength and durability. This mechanistic knowledge justifies the possibility of the development of high-performance, low-carbon non-fired bricks using industrial solid wastes by controlled hybrid activations.

3.7. Environmental impact and cost analysis of CNFSWB

Since CNFSWB is designed with all the industrial solid waste and does not need a high-temperature firing, it is important to determine its environmental and economic performance to prove its sustainability potential in construction applications. This paper has considered a life cycle analysis (LCA)-based methodology of determining the embodied carbon dioxide emissions (EC), embodied energy consumption (EE), and material cost of the designed CNFSWB system.

The embodied CO_2 emissions include the greenhouse gas emissions during the extraction and processing of the raw materials, the transportation and drying of the product, the calcination and sieving of the product. The embodied carbon of CNFSWB was determined using Eq. 8, which takes into consideration the mass contribution of each constituent material and the unit embodied CO_2 emission factor of that material. In the same way, the embodied energy consumption was calculated by presenting the energy intensity of individual raw materials by the use of the Eq. 9.

$$Embodied\ CO_2 = \sum_{i=1}^{n}(m_i \times CO_i); \quad (8)$$

where m_i is the mass per unit volume of each component, n is the total number of components in the binder system, and CO_i represents the embodied CO_2 emissions per unit mass of the material.

The embodied energy consumption was evaluated in a similar manner using:

$$Embodied\ CO_2 = \sum_{i=1}^{n}(m_i \times Energy_i). \quad (9)$$

The values of embodied carbon, embodied energy, and unit cost of OPC, RM, FA, SF, NaOH, and water used in this paper are shown in Table 6. These values are used to determine the overall environment and economic conditions of the composite brick system.

Table 6. EC and EE of raw materials and cost of raw materials

Raw materials	Embodied CO_2 emission, kg CO_2/kg	Embodied energy, MJ/kg	Material cost, HKD/kg	Ref.
OPC	0.83	5.75	0.918	[66-69]
RM	0.015	0	0	[70-72]
FA	0.01	0.10	0.35	[73]
SF	0.15	0.16	2.1	[68]
NaOH	0.625	4.98	2.73	[74]
H_2O	0.001	0.1	0.007	[74]
*The exchange rate of GBP-HKD was regarded as around 10.28.				

3.7.1. Embodied CO_2 emission

The materials made using OPC are particularly famous to be characterized by a high carbon footprint as a result of the exhaustive level of calcinations and the use of fossil fuels. Conversely, CNFSWB greatly minimizes the embodied carbon with the abundant use of industrial by-products, especially RM, FA, and SF, which are only slightly further processed.

OPC is the constituent with the greatest embodied CO_2 emission (0.83 kg CO_2/kg), as compared with RM and FA, which have insignificant carbon footprint because of the waste origin of these substances. Though alkaline activators, including NaOH, may have a rather high embodied carbon, the dosage used in CNFSWB is significantly reduced relative to traditional geopolymer systems, so the overall contribution is reduced.

Consequently, the overall embodied carbon of CNFSWB is significantly lower in comparison with the conventional fired clay bricks and OPC-based masonry units. The ratio between compressive strength and embodied carbon per MPa also demonstrates the higher carbon efficiency of CNFSWB, pointing out that the high mechanical performance is attained by a minimal environmental impact.

3.7.2. Embodied energy

This is the same case of embodied energy consumption of CNFSWB as embodied carbon. The embodied energy contribution is dominated by OPC and NaOH because they are energy-intensive to produce and RM and FA have almost zero embodied energy. One of the most crucial benefits of CNFSWB is the fact that this manufacturing route does not require energy input (either by kiln firing, sintering, or steam curing).

Therefore, the overall embodied energy of CNFSWB is still much less than the embodied energy of the fired bricks, UHPC, and cement-based masonry material in the literature. When compressive strength is taken into account, CNFSWB has shown a low embodied energy per MPa, indicating synergistic interaction between uniaxial compaction and chemical activation to obtain dense microstructures and high strength with low energy input.

3.7.3. Material cost analysis

CNFSWB material was assessed in terms of unit prices, provided in Table 6. RM was also assumed conservatively in that it has no cost, since the waste is an industrial waste that in most cases does not fetch commercial value, but costs in terms of disposal. FA and water also report very low costs, and SF and NaOH are the main contributors of the cost. Although alkaline activators are included, the total cost of CNFSWB can be considered competitive because firing energy is removed, and the level of OPC substitution with waste-derived materials is high. CNFSWB has a lower cost per unit volume than the traditional fired bricks and cement-based masonry units. More to the point, CNFSWB has a low material cost per MPa when normalized by compressive strength, which means that it is highly cost-efficient when it comes to the delivery of mechanical performance. This is a big edge, especially when it comes to applications that need high strength, durability and sustainability.

3.7.4. Sustainability implications

CNFSWB has a high potential as an alternative to the traditional masonry materials through its ability to be low embodied carbon and low embodied energy and at the same time be competitive on material costs, thus making it a sustainable material. These two properties of the combined application of industrial solid wastes and densification technology allow CNFSWB to be more efficient than conventional materials in the environment per unit strength. In general, the findings confirm that CNFSWB is a cost effective and resource efficient multi-purpose construction material, in addition to being an environmentally friendly resource with regard to the construction of infrastructural and building projects on a large scale.

4. CONCLUSIONS

The strength formation of compressed non-fired solid waste blocks (CNFSWB) made of RM, FA, and SF is controlled firstly by the chemical activation mechanism, and the physical compaction at 10 MPa has the most impact on the first-stage densification, but not effective for bonding.

Non-activated CNFSWB has a zero compressive strength, which proves the lack of any important self-cementing properties of the RM–FA–SF system without chemical activation. NaOH activation alone (AA–CNFSWB) triggers the dissolution of aluminosilicate and geopolymerization process, thus producing moderate strength, but the insufficient amount of calcium prevents further densification of the gel and long-term mechanical behavior.

The cement hydration-driven secondary pozzolanic reactions stabilize the strength evolution of the OPC-activated CNFSWB to a compressive strength of about 40 MPa in 28 days.

The activation of OPC with NaOH hybrid allows improving the mechanical performance significantly, allowing the simultaneous creation of C–(A)–S–H and N–(A)–S–H gels, which increases the homogeneous microstructure.

The optimal concentration of NaOH of 8.4 g (H3–CNFSWB) provides the maximum compressive strength of 28 days of 52.24 MPa, which demonstrates that there is good interaction between the alkali activation process and the cement hydration process. H3–CNFSWB and H4–CNFSWB samples were found to be of good freeze-thaw resistance (they showed negligible loss of strength and mass at repeated thawing-freezing cycles).

The lack of NaOH does not activate the aluminosilicate fully, and excessive alkalinity will have negative effects on the strength because the gel in alumina silicate will not polymerize properly and more micro structural defects will be formed.

The microstructural and phase analyses (XRD, FTIR, TG–DTG, and SEM) have continuously verified the gradual change of crystalline precursors to pure gel phases with the predominant ratio, i.e., hybrid activation, OPC activation, alkali activation, and compaction-only. These findings indicate that using controlled hybrid activation strategy, industrial solid wastes can be converted to high-strength, low-carbon non-fired construction blocks.

Acknowledgements

This work was supported by Shandong Provincial Natural Science Foundation Innovation and Development Joint Fund (ZR2025LGY011), the National Natural Science Foundation of China (Grant No. 22178339), 2023 Innovation-driven Development Special Foundation of Guangxi Province (AA23023021), the Hundred Talents Program (A) of the Chinese Academy of Sciences, and the University Science Research Project of Anhui Province (2022AH050076).

REFERENCES

1. **Fei, X., Fang, M., Wang, Y.** Climate Change Affects Land-disposed Waste *Nature Climate Change* 11 (12) 2021: pp. 1004 – 1005. https://doi.org/10.1038/s41558-021-01220-5
2. **Nriagu, J.O., Pacyna, J.M.** Quantitative Assessment of Worldwide Contamination of Air, Water and Soils By Trace Metals *Nature* 333 (6169) 1988: pp. 134 – 139. https://doi.org/10.1038/333134a0
3. **Sun, Z., Tao, Z., Li, H., Pittman, A.S., Zhou, F., Zhang, G., Cao, Y.** Recovery of Rare Earth Elements, Gallium and Germanium from Fly Ash and Red Mud Via Ultra-Fast Flash Joule Heating *Chemical Engineering Science* 2025: pp. 121879. https://doi.org/10.1016/j.ces.2025.121879
4. **Li, Z.** Toward Low-Carbon Construction: A Review of Red Mud Utilization in Cementitious Materials and Geopolymers for Sustainability and Cost Benefits *Buildings* 16 (2) 2026: pp. 362. https://doi.org/10.3390/buildings16020362
5. **Tang, L., He, Z., Yang, R., Pei, S., Zou, M., Qin, M.** High Temperature Calcined Red Mud-Cement Mortar: Workability, Mechanical Properties, Hydration Mechanism, and Microstructure *Sustainable Chemistry and Pharmacy* 41 2024: pp. 101717. https://doi.org/10.1016/j.scp.2024.101717
6. **Wei, C., Lu, Y., Liu, X., Zhang, Z., Wu, P., Gu, J.** Harmless Disposal Of Phosphogypsum Synergized Red Mud: Harmful Element Control and Material Utilization *Journal of Environmental Chemical Engineering* 12 (5) 2024: pp. 113660. https://doi.org/10.1016/j.jece.2024.113660
7. **Liu, Y., Zhang, L., Chen, L., Xue, B., Wang, G., Zhu, G., Yang, D.** Potential of Artificial Soil Preparation for Vegetation Restoration Using Red Mud and Phosphogypsum *Science of the Total Environment* 941 2024: pp. 173553. https://doi.org/10.1016/j.scitotenv.2024.173553
8. **Singh, S., Chattopadhyay, S.** Enhancing Self-Healing and Durability of High-Strength Concrete Using Bacterial-Induced Calcite Precipitation and Zeolite: An Experimental and Multi-Objective Optimization Approach *Asian Journal of Civil Engineering* 27 (4) 2026: pp. 1721 – 1738. https://doi.org/10.1007/s42107-025-01583-6
9. **Schramm, T., Neubauer, J. Goetz-Neunhoeffer, F.** Influence of Silica Fume Addition and Content on the Early Hydration of Calcium Aluminate Cement – The Role of Soluble Silicon *Cement and Concrete Research* 184 2024: pp. 107618. https://doi.org/10.1016/j.cemconres.2024.107618
10. **Singh, R.P., Vanapalli, K.R., Cheela, V. R.S., Peddireddy, S.R., Sharma, H.B., Mohanty, B.** Fly Ash, GGBS, and Silica Fume Based Geopolymer Concrete with Recycled Aggregates: Properties and Environmental Impacts *Construction and Building Materials* 378 2023: pp. 131168. https://doi.org/10.1016/j.conbuildmat.2023.131168
11. **Gao, M., Wang, J., Sha, W., Guo, Y.** Physico-Mechanical Properties and Synergistic Hydration Mechanism of Steel Slag-GBFS Based Alkali-Activated Composites Incorporated with Silica Fume *Journal of Materials Research and Technology* 36 2025: pp. 3327 – 3341. https://doi.org/10.1016/j.jmrt.2025.04.030
12. **Lin, M., Chen, G., Chen, Y., Han, D., Su, R., Wu, J.** Mechanical Properties and Microstructure of Fly Ash and Slag-Based Geopolymer Prepared by Silica Fume-Based Activator *Journal of Cleaner Production* 498 2025: pp. 145214. https://doi.org/10.1016/j.jclepro.2025.145214
13. **Gómez-Casero, M.A., Pérez-Villarejo, L., Sánchez-Soto, P.J., Eliche-Quesada, D.** Comparative Study of Alkali Activated Cements Based on Metallurgical Slags, in Terms of Technological Properties Developed *Journal* 29 2022: pp. 100746. http://dx.doi.org/10.1016/j.scp.2022.100746
14. **Freidin, C.** Cementless Pressed Blocks From Waste Products Of Coal-Firing Power Station *Construction and Building Materials* 21 (1) 2007: pp. 12 – 18. https://doi.org/10.1016/j.conbuildmat.2005.08.002
15. **Naganathan, S., Mohamed, A.Y.O., Mustapha, K.N.** Performance of Bricks Made Using Fly Ash and Bottom Ash *Construction and Building Materials* 96 2015: pp. 576 – 580. https://doi.org/10.1016/j.conbuildmat.2015.08.068
16. **Malhotra, S., Tehri, S.** Development Of Bricks From Granulated Blast Furnace Slag *Construction and Building Materials* 10 (3) 1996: pp. 191 – 193. https://doi.org/10.1016/0950-0618(95)00081-X
17. **Kazmi, S.M., Abbas, S., Saleem, M.A., Munir, M.J., Khitab, A.** Manufacturing of Sustainable Clay Bricks: Utilization of Waste Sugarcane Bagasse and Rice Husk Ashes *Construction and Building Materials* 120 2016: pp. 29 – 41. https://doi.org/10.1016/j.conbuildmat.2016.05.084
18. **Singh, S., Aswath, M., Ranganath, R.** Performance Assessment Of Bricks And Prisms: Red Mud Based Geopolymer Composite *Journal of Building Engineering* 32 2020: pp. 101462. https://doi.org/10.1016/j.jobe.2020.101462
19. **Tome, S., Nana, A., Tchakouté, H.K., Temuujin, J., Rüscher, C.H.** Mineralogical Evolution of Raw Materials Transformed to Geopolymer Materials: A Review *Ceramics International* 50 (19) 2024: pp. 35855 – 35868. https://doi.org/10.1016/j.ceramint.2024.07.024
20. **Boldyryev, S., Mikulčić, H., Mohorović, Z., Vujanović, M., Krajačić, G., Duić, N.** The Improved Heat Integration of Cement Production Under Limited Process Conditions: A Case Study for Croatia *Applied Thermal Engineering* 105 2016: pp. 839 – 848. https://doi.org/10.1016/j.applthermaleng.2016.05.139
21. **Wang, J., Liu, S., Zhao, X., Wu, K., Fang, J., Yu, H., Xu, L.** Carbon Sequestration In Relation To Cement Variety: Mechanical Properties, Microstructural Evolution And Carbon Footprint *Construction and Building Materials* 468 2025: pp. 140401. https://doi.org/10.1016/j.conbuildmat.2025.140401
22. **Wang, W.C., Lee, M.G., Deng, J.L., Wang, Y.C., Chuo, S.F., Pei-Chi, H., Jen-Wei, S.** Study on Carbon Sequestration and CO_2 Mixing of Fresh Cement Mortar *Case Studies in Construction Materials* 21 2024: pp. e03813. https://doi.org/10.1016/j.cscm.2024.e03813
23. **Yao, Z., Kashani, A., Rawal, A., Song, H., Kim, T.** Heat-Induced Phase Transitions in Mining Tailings to Create Alternative Supplementary Cementitious Materials *Resources, Conservation and Recycling* 210 2024: pp. 107818. https://doi.org/10.1016/j.resconrec.2024.107818

24. **Song, Y., Qian, J., Wang, Z., Wang, Z.** Self-Cementing Mechanism of CFBC Coal Ashes at Early Ages *Journal of Wuhan University of Technology-Mater. Sci. Ed.* 23 (3) 2008: pp. 338 – 341. https://doi.org/10.1007/s11595-007-3338-9
25. **Zhang, L., Chen, B.** Hydration And Properties Of Slag Cement Activated By Alkali And Sulfate *Journal of Materials in Civil Engineering* 29 (9) 2017: p. 04017091. https://doi.org/10.1061/(ASCE)MT.1943-5533.0001879
26. **Paris, J.M., Roessler, J.G., Ferraro, C.C., DeFord, H.D., & Townsend, T. G.** A Review of Waste Products Utilized as Supplements to Portland Cement in Concrete *Journal of Cleaner Production* 121 2016: pp. 1 – 18. https://doi.org/10.1016/j.jclepro.2016.02.013
27. **Bellmann, F., Stark, J.** Activation Of Blast Furnace Slag By A New Method *Cement and Concrete Research* 39 (8) 2009: pp. 644 – 650. https://doi.org/10.1016/j.cemconres.2009.05.012
28. **Sadique, M., Al-Nageim, H., Atherton, W., Seton, L., Dempster, N.** Mechano-Chemical Activation of High-Ca Fly Ash by Cement Free Blending and Gypsum Aided Grinding *Construction and Building Materials* 43 2013: pp. 480 – 489. https://doi.org/10.1016/j.conbuildmat.2013.02.050
29. **Sadique, M., Al Nageim, H., Atherton, W., Seton, L., Dempster, N.** A New Composite Cementitious Material for Construction *Construction and Building Materials* 36 2012: pp. 846 – 855. https://doi.org/10.1016/j.conbuildmat.2012.04.107
30. **Makhloufi, Z., Chettih, M., Bederina, M., Kadri, E.H., Bouhicha, M.** Effect of Quaternary Cementitious Systems Containing Limestone, Blast Furnace Slag and Natural Pozzolan on Mechanical Behavior of Limestone Mortars *Construction and Building Materials* 95 2015: pp. 647 – 657. https://doi.org/10.1016/j.conbuildmat.2015.07.050
31. **Shi, C., Jiménez, A.F., Palomo, A.** New Cements for the 21st Century: The Pursuit of an Alternative to Portland Cement *Cement and Concrete Research* 41 (7) 2011: pp. 750 – 763. https://doi.org/10.1016/j.cemconres.2011.03.016
32. **Blanco, F., Garcia, M.P., Ayala, J., Mayoral, G., Garcia, M. A.** The Effect of Mechanically and Chemically Activated Fly Ashes on Mortar Properties *Fuel* 85 (14 – 15) 2006: pp. 2018 – 2026. https://doi.org/10.1016/j.fuel.2006.03.031
33. **Velandia, D.F., Lynsdale, C.J., Provis, J.L., Ramirez, F., Gomez, A.C.** Evaluation of Activated High Volume Fly Ash Systems Using Na_2SO_4, Lime and Quicklime in Mortars with High Loss on Ignition Fly Ashes *Construction and Building Materials* 128 2016: p. 248 – 255. https://doi.org/10.1016/j.conbuildmat.2016.10.076
34. **Angulo-Ramírez, D.E., De Gutiérrez, R.M., Puertas, F.** Alkali-Activated Portland Blast-Furnace Slag Cement: Mechanical Properties and Hydration *Construction and Building Materials* 140 2017: pp. 119 – 128. https://doi.org/10.1016/j.conbuildmat.2017.02.092
35. **Phoo-Ngernkham, T., Hanjitsuwan, S., Damrongwiriyanupap, N., Chindaprasirt, P.** Effect of Sodium Hydroxide and Sodium Silicate Solutions on Strengths of Alkali Activated High Calcium Fly Ash Containing Portland Cement *KSCE Journal of Civil Engineering* 21 (6) 2017: pp. 2202 – 2210. https://doi.org/10.1007/s12205-016-0327-6
36. **Scrivener, K.L., Nonat, A.** Hydration of Cementitious Materials, Present and Future *Cement and Concrete Research* 41 (7) 2011: pp. 651 – 665. https://doi.org/10.1016/j.cemconres.2011.03.026
37. **Meinhard, K., Lackner, R.** Multi-Phase Hydration Model for Prediction of Hydration-Heat Release of Blended Cements *Cement and Concrete Research* 38 (6) 2008: pp. 794 – 802. https://doi.org/10.1016/j.cemconres.2008.01.008
38. **Komnitsas, K., Zaharaki, D.** Geopolymerisation: A Review and Prospects for the Minerals Industry *Minerals Engineering* 20 (14) 2007: pp. 1261 – 1277. https://doi.org/10.1016/j.mineng.2007.07.011
39. **Shi, Z., Shi, C., Wan, S., Ou, Z.** Effect of Alkali Dosage on Alkali-Silica Reaction in Sodium Hydroxide Activated Slag Mortars *Construction and Building Materials* 143 2017: pp. 16 – 23. https://doi.org/10.1016/j.conbuildmat.2017.03.125
40. **Shi, Z., Shi, C., Wan, S., Zhang, Z.** Effects of Alkali Dosage and Silicate Modulus on Alkali-Silica Reaction in Alkali-Activated Slag Mortars *Cement and Concrete Research* 111 2018: pp. 104 – 115. https://doi.org/10.1016/j.cemconres.2018.06.005
41. **Qian, J., Shi, C., Wang, Z.** Activation of Blended Cements Containing Fly Ash *Cement and Concrete Research* 31 (8) 2001: pp. 1121 – 1127. https://doi.org/10.1016/S0008-8846(01)00526-9
42. **Burciaga-Díaz, O., Betancourt-Castillo, I.** Characterization of Novel Blast-Furnace Slag Cement Pastes and Mortars Activated with a Reactive Mixture of MgO-NaoH *Cement and Concrete Research* 105 2018: pp. 54 – 63. https://doi.org/10.1016/j.cemconres.2018.01.002
43. **Ozturk, S., Sutcu, M., Erdogmus, E., Gencel, O.** Influence of Tea Waste Concentration in the Physical, Mechanical and Thermal Properties of Brick Clay Mixtures *Construction and Building Materials* 217 2019: pp. 592 – 599. https://doi.org/10.1016/j.conbuildmat.2019.05.114
44. **Reddy, B.V., Jagadish, K.** Embodied Energy of Common and Alternative Building Materials And Technologies *Energy and Buildings* 35 (2) 2003: pp. 129 – 137. https://doi.org/10.1016/j.conbuildmat.2019.05.114
45. **Velasco, P.M., Ortíz, M.M., Giró, M.M., Velasco, L.M.** Fired Clay Bricks Manufactured by Adding Wastes as Sustainable Construction Material – A Review *Construction and Building Materials* 63 2014: pp. 97 – 107. https://doi.org/10.1016/j.conbuildmat.2014.03.045
46. **Raut, S., Ralegaonkar, R., Mandavgane, S.** Development of Sustainable Construction Material Using Industrial and Agricultural Solid Waste: A Review of Waste-Create Bricks *Construction and Building Materials* 25 (10) 2011: pp. 4037 – 4042. https://doi.org/10.1016/j.conbuildmat.2011.04.038
47. **Zhang, L.** Production of Bricks from Waste Materials – A Review *Construction and Building Materials* 47 2013: pp. 643 – 655. https://doi.org/10.1016/j.conbuildmat.2013.05.043
48. **Cheah, C.B., Part, W.K., Ramli, M.** The Long Term Engineering Properties of Cementless Building Block Work Containing Large Volume of Wood Ash and Coal Fly Ash *Construction and Building Materials* 143 2017: pp. 522 – 536. https://doi.org/10.1016/j.conbuildmat.2017.03.162
49. **Chinese Standard GB/T 17671-2021.** Test Method of Cement Mortar Strength (ISO Method). State Market Regulatory Administration: Beijing, China, 2021.
50. **Ashraf, W., Olek, J.** Carbonation Behavior of Hydraulic and Non-Hydraulic Calcium Silicates: Potential Of Utilizing Low-Lime Calcium Silicates in Cement-Based Materials *Journal of Materials Science* 51 (13) 2016: pp. 6173 – 6191. https://doi.org/10.1007/s10853-016-9909-4
51. **Bakharev, T.** Durability Of Geopolymer Materials In Sodium And Magnesium Sulfate Solutions *Cement and Concrete Research* 35 (6) 2005: pp. 1233 – 1246. https://doi.org/10.1016/j.cemconres.2004.09.002

52. **Tu, W., Fang, G., Dong, B., Zhang, M.** Multiscale Study of Microstructural Evolution in Alkali-Activated Fly Ash-Slag Paste at Elevated Temperatures *Cement and Concrete Composites* 143 2023: pp. 105258. https://doi.org/10.1016/j.cemconcomp.2023.105258
53. **Zhang, J., Shi, C., Zhang, Z.** Carbonation Induced Phase Evolution in Alkali-Activated Slag/Fly Ash Cements: The Effect of Silicate Modulus of Activators *Construction and Building Materials* 223 2019: pp. 566 – 582. https://doi.org/10.1016/j.conbuildmat.2019.07.024
54. **Silva, A.M.B., Queiroz, C.M., Agathopoulos, S., Correia, R.N., Fernandes, M.H.V., Oliveira, J.M.** Structure of SiO_2–MgO–Na_2O Glasses By FTIR, Raman and 29Si MAS NMR *Journal of Molecular Structure* 986 (1 – 3) 2011: pp. 16 – 21. https://doi.org/10.1016/j.molstruc.2010.11.023
55. **Li, J., Tao, Y., Zhuang, E., Cui, X., Yu, K., Yu, B., Yi, C.** Optimal Amorphous Oxide Ratios and Multifactor Models for Binary Geopolymers from Metakaolin Blended with Substantial Sugarcane Bagasse Ash *Journal of Cleaner Production* 377 2022: pp. 134215. https://doi.org/10.1016/j.jclepro.2022.134215
56. **Ge, X., Hu, X., Shi, C.** Mechanical Properties and Microstructure of Circulating Fluidized Bed Fly Ash and Red Mud-Based Geopolymer *Construction and Building Materials* 340 2022: pp. 127599. https://doi.org/10.1016/j.conbuildmat.2022.127599
57. **Yang, N., Xue, S., Ahmad, M.R., Xuan, Q., Kai, M.F., Dai, J.G.** Development of Red Mud-Modified Geopolymer Coating with Radiative Cooling Effect for Footway Application *Journal of Cleaner Production* 450 2024: pp. 141915. https://doi.org/10.1016/j.jclepro.2024.141915
58. **Shi, Y., Zhao, Q., Xue, C., Jia, Y., Guo, W., Zhang, Y., Qiu, Y.** Preparation and Curing Method of Red Mud-Calcium Carbide Slag Synergistically Activated Fly Ash-Ground Granulated Blast Furnace Slag Based Eco-Friendly Geopolymer *Cement and Concrete Composites* 139 2023: pp. 104999. https://doi.org/10.1016/j.cemconcomp.2023.104999
59. **Wang, X., Qi, J., Zhu, H., Wang, J., Zeng, H., Li, B., Yan, S.** Enhanced Sequestration of CO_2 from Simulated Electrolytic Aluminum Flue Gas by Modified Red Mud *Journal of Environmental Management* 346 2023: pp. 118972. https://doi.org/10.1016/j.jenvman.2023.118972
60. **Ke, G., Li, Z., Jiang, H.** Study on Long-Term Solidification of All-Solid Waste Cementitious Materials Based on Circulating Fluidized Bed Fly Ash, Red Mud, Carbide Slag, and Fly Ash *Construction and Building Materials* 427 2024: pp. 136284. https://doi.org/10.1016/j.conbuildmat.2024.136284
61. **Liu, Y., Zhuge, Y., Chen, X., Duan, W., Fan, R., Outhred, L., Wang, L.** Miro-Chemomechanical Properties of Red Mud Binder and its Effect on Concrete *Composites Part B: Engineering* 258 2023: pp. 110688. https://doi.org/10.1016/j.compositesb.2023.110688
62. **Cui, W., Dong, X., Duan, W., Liu, J., Zhao, R., He, G.** Design of All Solid Waste Red Mud-Based Cementitious Materials Based on the Simplex Centroid Method *Construction and Building Materials* 418 2024: pp. 135439. https://doi.org/10.1016/j.conbuildmat.2024.135439
63. **Yan, Z., Li, H., Zhang, L.** CO_2 Activation of Magnesium Slag for the Preparation of Unburned Aggregate: Peormance Evaluation, CO_2 Absorption, and Ecological Benefits *Construction and Building Materials* 445 2024: pp. 137905. https://doi.org/10.1016/j.conbuildmat.2024.137905
64. **Zhang, Q., Feng, P., Shen, X., Cai, Y., Zhen, H., Liu, Z.** Comparative Analysis of Carbonation Strengthening Mechanisms in Full Solid Waste Materials: Steel Slag vs. Carbide Slag *Cement and Concrete Composites* 157 2025: pp. 105927. https://doi.org/10.1016/j.cemconcomp.2025.105927
65. **von Greve-Dierfeld, S., Lothenbach, B., Vollpracht, A., Wu, B., Huet, B., Andrade, C., De Belie, N.** Understanding the Carbonation of Concrete with Supplementary Cementitious Materials: A Critical Review by Rilem TC 281-CCC *Materials and Structures* 53 (6) 2020: po. 136. https://doi.org/10.1617/s11527-020-01558-w
66. **Baur, I., Ludwig, C., Johnson, C.A.** The Leaching Behavior of Cement Stabilized Air Pollution Control Residues: A Comparison of Field and Laboratory Investigations *Environmental Science & Technology*, 35 (13) 2001: pp. 2817 – 2822. https://doi.org/10.1021/es000243r
67. **Chen, P., Wang, C., Wang, Y., Xie, J., Shen, X., Wang, C., Wang, J.** Pre-Carbonation of Calcium Carbide Slag for the Preparation of Eco-Friendly Mortars *Construction and Building Materials* 399 2023: pp. 132541. https://doi.org/10.1016/j.conbuildmat.2023.132541
68. **Liu, J., Li, M., Jin, H., Cheng, L., Xing, F.** The Role of Different Ratios of Biochar in the Artificial Lightweight Cold-Bonded Aggregates (ALCBAS) Containing High Volume of Red Mud (RM) *Construction and Building Materials* 422 2024: pp. 135815. https://doi.org/10.1016/j.conbuildmat.2024.135815
69. **Shi, J., Liu, Y., Li, Z., Lei, J., Yin, K., Zhang, Z., Xie, N.** Upcycling Use of Red Mud-Based Solid Waste In Engineered Cementitious Composites: Properties, Activation Mechanism, and Life-Cycle Assessment *Journal of Cleaner Production* 447 2024: pp. 141504. https://doi.org/10.1016/j.jclepro.2024.141504
70. **Qian, L.P., Ahmad, M.R., Lao, J.C., Dai, J. G.** Recycling of Red Mud and Flue Gas Residues in Geopolymer Aggregates (GPA) for Sustainable Concrete *Resources, Conservation and Recycling* 191 2023: pp. 106893. https://doi.org/10.1016/j.resconrec.2023.106893
71. **Manjunatha, M., Preethi, S., Mounika, H.G., Niveditha, K.N.** Life Cycle Assessment (LCA) of Concrete Prepared with Sustainable Cement-Based Materials *Materials Today: Proceedings* 47 2021: pp. 3637 – 3644. https://doi.org/10.1016/j.matpr.2021.01.248
72. **Lao, J.C., Ma, R.Y., Xu, L.Y., Li, Y., Shen, Y.N., Yao, J., Huang, B.T.** Fly Ash-Dominated High-Strength Engineered/Strain-Hardening Geopolymer Composites (HS-EGC/SHGC): Influence of Alkalinity and Environmental Assessment *Journal of Cleaner Production* 447 2024: pp. 141182. https://doi.org/10.1016/j.jclepro.2024.141182